Simultaneous whole-animal 3D imaging of neuronal activity using light-field microscopy

Robert Prevedel[1–3,10], Young-Gyu Yoon[4,5,10], Maximilian Hoffmann[1–3], Nikita Pak[5,6], Gordon Wetzstein[5], Saul Kato[1], Tina Schrödel[1], Ramesh Raskar[5], Manuel Zimmer[1], Edward S Boyden[5,7–9] & Alipasha Vaziri[1–3]

High-speed, large-scale three-dimensional (3D) imaging of neuronal activity poses a major challenge in neuroscience. Here we demonstrate simultaneous functional imaging of neuronal activity at single-neuron resolution in an entire *Caenorhabditis elegans* and in larval zebrafish brain. Our technique captures the dynamics of spiking neurons in volumes of ~700 μm × 700 μm × 200 μm at 20 Hz. Its simplicity makes it an attractive tool for high-speed volumetric calcium imaging.

Understanding how sensory inputs are dynamically mapped onto the functional activity of neuronal populations and how their processing leads to cognitive functions and behavior requires tools for non-invasive interrogation of neuronal circuits with high spatiotemporal resolution[1,2]. A number of approaches for 3D neural activity imaging that take advantage of chemical and genetically encoded fluorescent reporters exist[3,4]. Whereas some are based on scanning the excitation light in a volume, either sequentially[5–7] or randomly[8,9], others try to capture 3D image data simultaneously by mapping axial information onto a single lateral plane using a range of approaches[10–14].

Light-field microscopy (LFM)[12] is one such simultaneous 3D imaging method that has been applied to nonbiological and fixed biological samples[12,13]. In contrast to conventional imaging schemes, a light-field microscope captures both the 2D location and 2D angle of the incident light. This is done by placing a microlens array in the native image plane such that sensor pixels capture the rays of the light field simultaneously. Such 4D light fields allow the synthesis of a focal stack computationally. In LFM, single sensor images are used to retrieve information for the entire 3D volume, a scheme that enables high-speed volumetric acquisition. However, despite its potentially superb temporal resolution, LFM has not to date been used for functional biological imaging. This is because capturing the 4D light-field information via a single sensor image comes at the cost of reduced spatial resolution and because of inherent trade-offs between axial imaging range and the spatial and axial resolution[12].

Here we report that neural tissues expressing calcium sensors can be imaged at volume rates of up to 50 Hz and at single-neuron resolution, using a 3D deconvolution algorithm[15,16] applied to LFM. We achieved effective resolutions up to ~1.4 μm and 2.6 μm in the lateral and axial dimensions, respectively, inside biological samples. To build our light-field deconvolution microscope (LFDM), we placed a microlens array at the image plane of an epifluorescence microscope (**Fig. 1a** and Online Methods), which captured the different perspectives of the sample (**Fig. 1b**) on the camera sensor. To overcome the trade-off between axial and lateral spatial resolution in LFM[12], we exploited aliasing of the recorded data and used computational reconstruction methods based on 3D deconvolution to effectively obtain improved lateral and axial resolution[15,16] (Online Methods, **Supplementary Notes 1** and **2** and **Supplementary Software**).

To evaluate the spatial resolution of our LFDM, we imaged subdiffraction-sized beads and reconstructed the point spread function (PSF) of our system (**Fig. 1b,c**). Using a 40× objective, we found resolutions of ~1.4 μm and 2.6 μm in the lateral and axial dimensions, respectively. To verify the suitability of the LFDM for capturing the activity of individual neurons, we imaged a sample consisting of 6-μm-diameter fluorescent beads randomly distributed in three dimensions in agarose and compared a conventional focal stack (taken without microlenses) (**Fig. 1d,e**) with the deconvolved light-field images (**Fig. 1f,g**).

Using the same objective with *C. elegans*, we were able to image the majority of a worm (~350 μm × 350 μm × 30 μm) while maintaining single-neuron resolution (**Fig. 2a–c**, **Supplementary Figs. 1–4** and **Supplementary Videos 1–5**). We could record activity of neurons in the brain region surrounding the nerve ring and the ventral cord at a 5-Hz volume rate. We note that our LFDM allows for substantially higher volume rates than this, which we demonstrated by recording unrestrained worms at 50 Hz (**Supplementary Fig. 4** and **Supplementary Video 3**). Such volume rates would in principle be sufficient for performing whole-brain imaging in freely moving worms, especially if additional tracking is employed as previously shown for single neurons[17]. However, as Ca^{2+} signals in *C. elegans* typically occur at timescales of up to 1 Hz, we chose
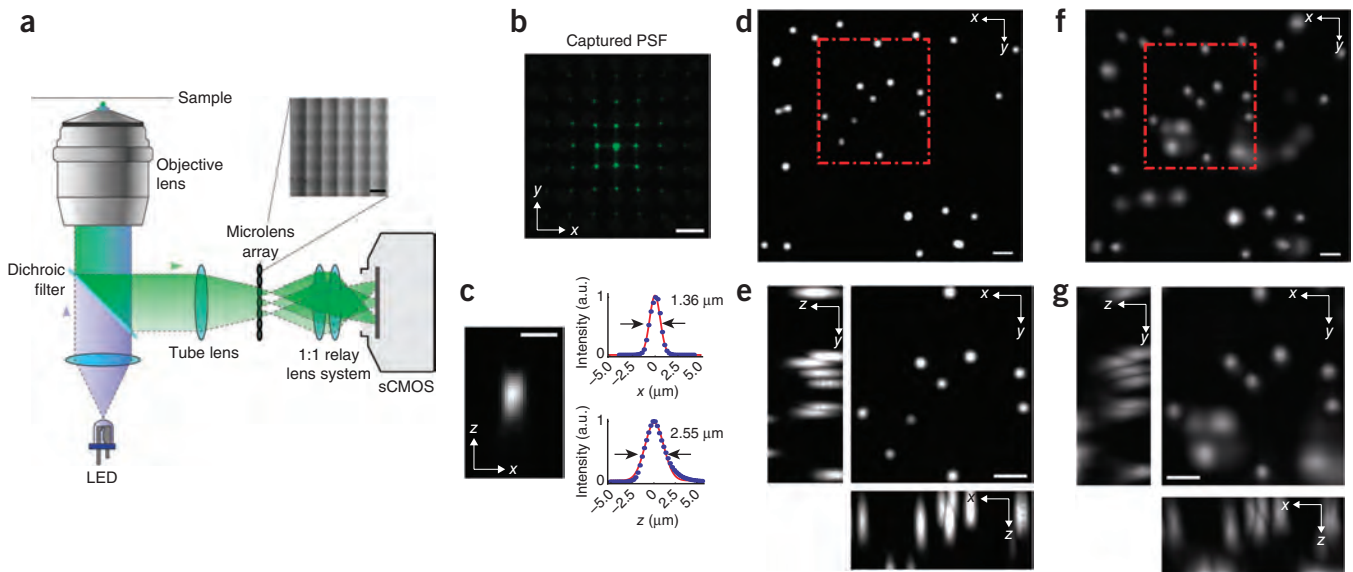
Figure 1 | Light-field deconvolution microscopy. (**a**) A microlens array was appended to the camera port of a wide-field microscope and placed in the primary image plane of the fluorescence microscope. The array itself was imaged with a 1:1 relay lens system onto the chip of a scientific complementary metal-oxide semiconductor (sCMOS) camera (Online Methods). Inset, close-up of the microlens array. (**b**) Point spread function (PSF) of a subdiffraction-sized bead located at $z = 7.5$ μm off the focal plane, as seen through the microlens array. (**c**) Axial (xz) PSF at $z = 7.5$ μm, reconstructed using the LFDM, and corresponding x and z profiles showing lateral and axial resolution, respectively. a.u., arbitrary units. (**d**) Maximum-intensity projection (MIP) of a deconvolved wide-field focal stack taken without microlenses. The sample consists of 6-μm-sized fluorescent beads in agarose. (**e**) Red box in **d**; xz- and yz-section MIPs are shown. (**f,g**) Corresponding volume of the same beads in **d,e**, 4–28 μm off the focal plane, reconstructed via 15 iterations of the light-field deconvolution algorithm. Scale bars, 150 μm (**a,b**), 3 μm (**c**) and 10 μm (**d–g**).

slower volume rates (5 Hz) in order to maximize the signal-to-noise ratio and reduce potential photobleaching.

The wide field of view (FOV) of the LFDM and the intrinsic simultaneity of the acquisition allow one to study correlations in activity of neurons across the whole animal, which would not be feasible with other unbiased Ca^{2+}-imaging techniques. In our experiments, we observed correlated and anticorrelated activity patterns between the premotor interneurons in the head and motor neurons located along the ventral nerve cord, which connect to body-wall muscles according to the WormAtlas (**Fig. 2a–c**).

We used the location, morphology and activity patterns of some of these neurons to identify specific premotor interneuron classes such as AVA, AVE, RIM, AIB and AVB, and A- and B-class motor neurons that have been associated with motor-program selection[18] (**Supplementary Fig. 3**). AVA neurons have been associated with a switch from forward to backward directed crawling, which depends on A-class motor neurons[19] and is associated with a change in the relative activities of A- and B-class motor neurons[18]. What we observed was consistent with these findings: a high correlation of AVA and A-class motor neuron activity and an anticorrelation of AVA and B-class motor neuron activity. Further, we used the LDFM and sensory stimulation to identify neuron classes (**Supplementary Fig. 3** and **Supplementary Video 5**). Applying consecutive 30-s intervals of high and low oxygen levels, we observed two neuron classes with increasing Ca^{2+} transients upon oxygen up- and downshift, respectively. Morphology, location and activity patterns of these neuron classes matched those of the oxygen chemosensory neurons BAG and URX[5].

We also recorded exclusively from brain regions surrounding the nerve ring (**Fig. 2d–f** and **Supplementary Fig. 2**). Imaging

smaller FOVs (~200 μm × 70 μm × 30 μm) led to faster volume reconstructions and better image quality owing to the lack of undesired fluorescence from coelomocytes, which were partially labeled in our transgenes. Similarly to previous findings[5], we were able to resolve up to 74 individual neurons in a typical recording, around 30 of which showed pronounced activity over the recording time of 200 s (**Fig. 2d–f** and **Supplementary Fig. 2**).

In order to highlight the temporal resolution and the broader applicability of our technique for capturing dynamics of large populations of spiking neurons, we performed Ca^{2+} imaging in live zebrafish larvae brains expressing the Ca^{2+} indicator GCaMP5 pan-neuronally. Employing a 20× objective, we demonstrated whole-brain Ca^{2+} imaging for volumes spanning ~700 μm × 700 μm × 200 μm at a 20-Hz volume rate. Although in this case optical single-cell resolution had to be compromised in favor of larger FOVs, we could still recover spatially resolved cellular signals over the entire time series using standard signal extraction and unmixing techniques[20]. Implementing this approach, we extracted neuronal activity for ~5,000 cells across the brain and followed their fast Ca^{2+} transients on a millisecond timescale (**Fig. 3** and **Supplementary Video 6**).

By applying an aversive odor to the fish (Online Methods), we evoked neuronal activity and inferred dynamics of Ca^{2+} signals across the olfactory system, the midbrain and parts of the hindbrain, results consistent with previous demonstrations of the neuronal dynamics in these regions[6,7,21–23]. The high temporal resolution of the LFDM revealed subtle differences in the exact timing of the onset of the response for different groups of neurons located close to each other (**Fig. 3c**). Whereas the neurons in each group exhibited a nearly synchronous onset of their activity,

Figure 2 | Whole-animal Ca^{2+} imaging of *C. elegans* using LFDM. (**a**) Wide-field image of the worm inside a microfluidic poly(dimethylsiloxane) (PDMS) device used for immobilization. The head is at the bottom right. (**b**) Maximum-intensity projection (MIP) of a light-field deconvolved image (15 iterations) containing 14 distinct *z* planes. Arrows and numbers indicate individual neurons in the head ganglia and ventral cord. (**c**) Ca^{2+} intensity traces ($\Delta F/F_0$) of NLS-GCaMP5K fluorescence of selected neurons as marked in **b** and imaged volumetrically at 5 Hz for 200 s (**Supplementary Video 1**). (**d**) Close-up of the brain region, with the MIP of the *xy* plane as well as *xz* and *yz* cross-sections indicated by the dashed lines (**Supplementary Video 2**). (**e**) Individual *z* planes of a typical recording of the worm's brain, reconstructed from a single camera exposure (see **Supplementary Fig. 2** for neuron IDs). In this recording, the worm's center along the lateral (left–right) (*z*) axis was placed at the focal plane of the objective. (**f**) Activity of all 74 neurons identified in **e** (**Supplementary Video 4**). Each row shows a time-series heat map of an individual neuron. Color indicates percent fluorescence changes ($\Delta F/F_0$); scaling is indicated by the color bar on the right. Scale bars, 50 μm (**b**,**e**), 10 μm (**d**).
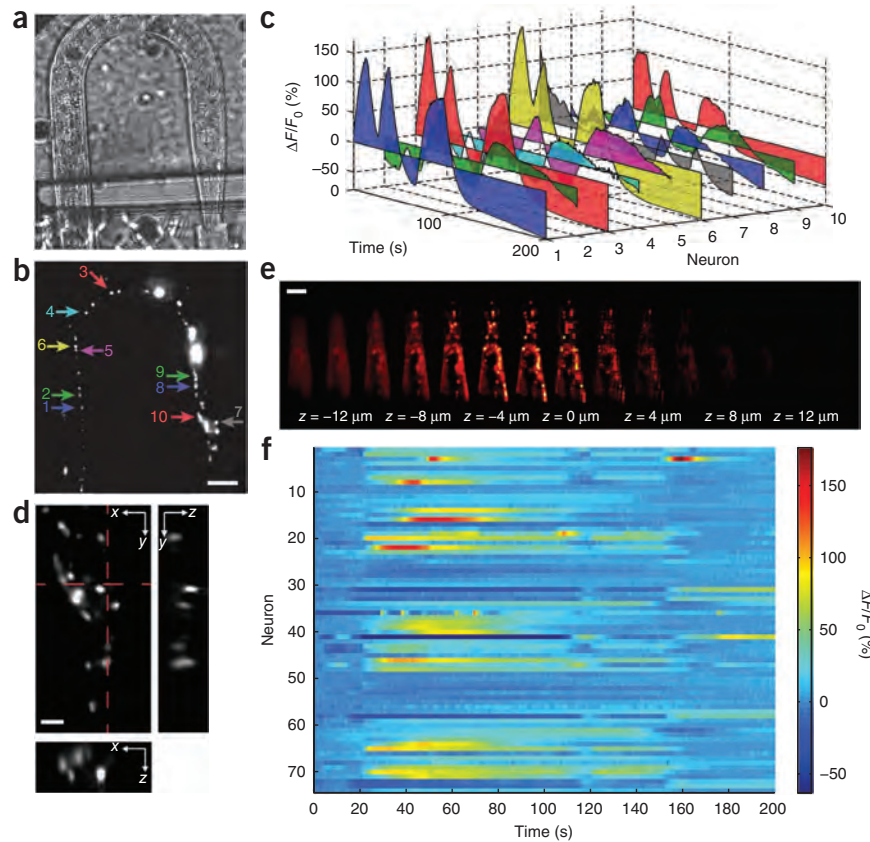
the collective response of each group was delayed with respect to those of the other groups. Overall, our imaging speed, which was more than an order of magnitude faster than in previous whole-brain functional imaging[6,7], was thus able to reliably capture the dynamic activity of a large number of cells with high spatial and temporal resolution.

In summary, we have implemented an LFDM and demonstrated its ability to capture the neuronal activity of the entire nervous system of *C. elegans* simultaneously at single-cell resolution as well as record dynamics of spiking neurons by performing whole-brain Ca[+2] imaging in larval zebrafish at 20 Hz. The increase in spatial resolution compared to that of LFM was achieved by performing deconvolution during postprocessing. The simultaneity of acquisition of volumes in LFDM imaging eliminates spatiotemporal ambiguity associated with sequentially recorded approaches and decouples temporal resolution from volume size. Resolutions in all three dimensions are set by the objective and microlens properties, and FOV and acquisition rate are determined by the camera chip size, frame rates and signal intensity. The LFDM is easy to set up and is cost effective and compatible with standard microscopes. Both the temporal resolution and the obtainable FOVs make light-field deconvolution microscopy an attractive technique for future combination with behavioral studies. Future work will focus on obtaining higher spatial resolutions and larger FOVs as well as faster and more efficient computational reconstruction techniques, both of which of are expected to improve with technological advancements in camera sensors and processors. Finally, the use of red-shifted Ca^{2+} sensors[24] and the combination of the LFDM with techniques for imaging at depth in biological tissue[25] bears further potential for widespread use of this method.

METHODS

Methods and any associated references are available in the online version of the paper.

Note: Any Supplementary Information and Source Data files are available in the online version of the paper.

AUTHOR CONTRIBUTIONS
R.P. designed microlenses, built the imaging system and performed experiments together with M.H. Y.-G.Y. designed and wrote 3D-deconvolution software with contributions from G.W. under the guidance of R.R. R.P. and M.H. refined and rebuilt the imaging system and analyzed data together with Y.-G.Y. N.P. implemented and tested the LFDM prototype. T.S. generated transgenic animals, provided microfluidic devices and performed cell identifications under the guidance of M.Z. S.K. wrote analysis software.
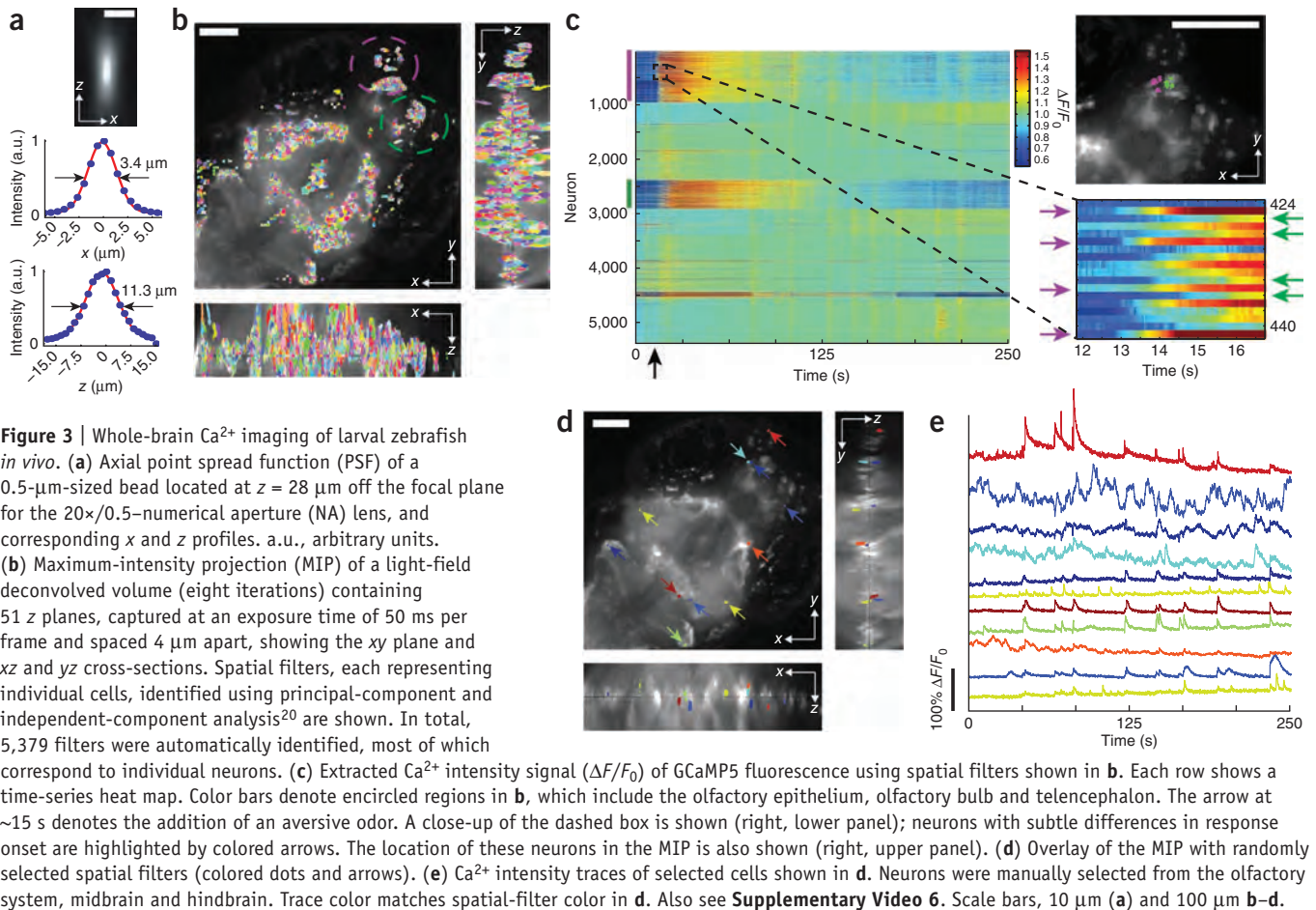
Figure 3 | Whole-brain Ca²⁺ imaging of larval zebrafish *in vivo*. (**a**) Axial point spread function (PSF) of a 0.5-μm-sized bead located at $z = 28$ μm off the focal plane for the 20×/0.5–numerical aperture (NA) lens, and corresponding x and z profiles. a.u., arbitrary units. (**b**) Maximum-intensity projection (MIP) of a light-field deconvolved volume (eight iterations) containing 51 z planes, captured at an exposure time of 50 ms per frame and spaced 4 μm apart, showing the xy plane and xz and yz cross-sections. Spatial filters, each representing individual cells, identified using principal-component and independent-component analysis[20] are shown. In total, 5,379 filters were automatically identified, most of which correspond to individual neurons. (**c**) Extracted Ca²⁺ intensity signal ($\Delta F/F_0$) of GCaMP5 fluorescence using spatial filters shown in **b**. Each row shows a time-series heat map. Color bars denote encircled regions in **b**, which include the olfactory epithelium, olfactory bulb and telencephalon. The arrow at ~15 s denotes the addition of an aversive odor. A close-up of the dashed box is shown (right, lower panel); neurons with subtle differences in response onset are highlighted by colored arrows. The location of these neurons in the MIP is also shown (right, upper panel). (**d**) Overlay of the MIP with randomly selected spatial filters (colored dots and arrows). (**e**) Ca²⁺ intensity traces of selected cells shown in **d**. Neurons were manually selected from the olfactory system, midbrain and hindbrain. Trace color matches spatial-filter color in **d**. Also see **Supplementary Video 6**. Scale bars, 10 μm (**a**) and 100 μm **b**–**d**.

1. Alivisatos, A.P. *et al. Neuron* **74**, 970–974 (2012).
2. Marblestone, A.H. *et al. Front. Comput. Neurosci.* **7**, 137 (2013).
3. Stosiek, C., Garaschuk, O., Holthoff, K. & Konnerth, A. *Proc. Natl. Acad. Sci. USA* **100**, 7319–7324 (2003).
4. Chen, T.-W. *et al. Nature* **499**, 295–300 (2013).
5. Schrödel, T., Prevedel, R., Aumayr, K., Zimmer, M. & Vaziri, A. *Nat. Methods* **10**, 1013–1020 (2013).
6. Ahrens, M.B., Orger, M.B., Robson, D.N., Li, J.M. & Keller, P.J. *Nat. Methods* **10**, 413–420 (2013).
7. Panier, T. *et al. Front. Neural Circuits* **7**, 65 (2013).
8. Duemani Reddy, G., Kelleher, K., Fink, R. & Saggau, P. *Nat. Neurosci.* **11**, 713–720 (2008).
9. Grewe, B.F., Langer, D., Kasper, H., Kampa, B.M. & Helmchen, F. *Nat. Methods* **7**, 399–405 (2010).
10. Cheng, A., Gonçalves, J.T., Golshani, P., Arisaka, K. & Portera-Cailliau, C. *Nat. Methods* **8**, 139–142 (2011).
11. Abrahamsson, S. *et al. Nat. Methods* **10**, 60–63 (2013).
12. Levoy, M., Ng, R., Adams, A., Footer, M. & Horowitz, M. *ACM Trans. Graph.* **25**, 924–934 (2006).
13. Levoy, M., Zhang, Z. & McDowall, I. *J. Microsc.* **235**, 144–162 (2009).
14. Quirin, S., Peterka, D.S. & Yuste, R. *Opt. Express* **21**, 16007–16021 (2013).
15. Agard, D.A. *Annu. Rev. Biophys. Bioeng.* **13**, 191–219 (1984).
16. Broxton, M. *et al. Opt. Express* **21**, 25418–25439 (2013).
17. Faumont, S. *et al. PLoS ONE* **6**, e24666 (2011).
18. Kawano, T. *et al. Neuron* **72**, 572–586 (2011).
19. Chalfie, M. *et al. J. Neurosci.* **5**, 956–964 (1985).
20. Mukamel, E.A., Nimmerjahn, A. & Schnitzer, M.J. *Neuron* **63**, 747–760 (2009).
21. Friedrich, R.W. & Korsching, S.I. *Neuron* **18**, 737–752 (1997).
22. Renninger, S.L. & Orger, M.B. *Methods* **62**, 255–267 (2013).
23. Jetti, S.K., Vendrell-Llopis, N. & Yaksi, E. *Curr. Biol.* **24**, 434–439 (2014).
24. Akerboom, J. *et al. Front. Mol. Neurosci.* **6**, 2 (2013).
25. Ntziachristos, V. *Nat. Methods* **7**, 603–614 (2010).

ONLINE METHODS

Setup. The LFM system is appended to an epifluorescence micro-scope (Zeiss, Axiovert 200) equipped with an LED excitation light source (λ = 465 nm, 300 mW, CoolLED) and a standard GFP filter set (Zeiss). In all *C. elegans* imaging experiments, we used a 40×/0.95-NA dry objective (Zeiss Apochromat), whereas zebrafish imaging was performed with a 20×/0.5-NA dry objective (Zeiss Plan-Neofluar). The microlens array is mounted inside a five-axis kinematic mount (Thorlabs) to allow fine adjustment of the array orthogonal to the optics axis, which we found crucial for high-quality results. The array is further imaged onto a 5.5-megapixel (2,560 × 2,160 pixels) sCMOS camera (Andor Zyla) using a 1:1 relay macro lens objective (Nikon AF-S 105mm 2.8 G VR IF-ED Micro) (**Fig. 1a**). Details on optical design choices and their effect on resolution are discussed in **Supplementary Note 1**.

***C. elegans* experiments.** To record neuronal activity from *C. elegans*, we loaded adult worms (1- to 4-egg stage) express-ing NLS-GCaMP5K under the *unc-31* promoter (strains ZIM294 and ZIM617) into a microfluidic channel that was connected to a reservoir containing S-basal buffer with 5 mM tetramisole, an acetylcholine receptor–specific agonist that mildly paralyzes the animal's muscles to reduce motion[5]. The worm was placed off the native focal plane and toward the objective using a piezo stepper motor (PI-721, Physik Instrumente) such that the entire worm was ideally contained in the region spanning -30 μm to 0 μm. By doing so, we exploited the highest resolution of LFDM while avoiding artifacts near the focal plane. When we recorded from the head region only, the worm's head ganglia were placed at the center of the FOV, and excitation was limited to this area by the use of an iris in the excitation pathway. For the experiments involving chemosensory stimulation, we followed the proce-dure described in ref. 5. Neurons were identified by classifica-tion according to size, shape and relative positions of cell nuclei using the WormAtlas[26]; previously described characteristic activ-ity patterns[5] were used as further confirmations. AVA neurons are located in the anterior-ventral part of the lateral ganglia and exhibit an elongated nucleus. AVE neurons are situated posteriorly-medially to AVA and have a similar activity pattern[18]. RIM neu-rons are located in the posterior ventral part of the lateral ganglia; their position is often ambiguous with that of RIB and AIB neu-rons, which also exhibit activity patterns similar to RIM. VB01 is located in the anterior-to-middle part of the retrovesicular gan-glion; its position is ambiguous with other motor neurons in this region such as DB02. DA01 is located at the posterior end of the retrovesicular ganglion. AVB neurons are located central to the lateral ganglia and typically show anticorrelated activity with that of AVA. Ambiguities are posed by the nearby neurons AIN, AVD, AVH and AVJ. BAG neurons are located at the posterior end of the anterior ganglion and exhibit the largest cell nucleus in this region; they reliably respond to oxygen downshift. URX neurons are located at the anterior dorsal end of the lateral ganglia directly ventrally to the unambiguously identifiable nucleus of ALA. URX neurons reliably respond to oxygen upshift.

Zebrafish larvae experiments. For zebrafish experiments, *mitfa*$^{-/-}$ larvae with pan-neuronal GCaMP5 expression have been imaged 5–8 d.p.f. (days post fertilization) using stable lines HuC:GCaMP5G and HuC:Gal4/UAS:GCaMP5G. We immobilized fish by embedding them in 2% agarose with the mouth and tail cleared of agarose to allow for odor stimulation and tail movement. Odor stimulation was performed during imaging by manually supply-ing decomposed fish water (an intrinsically aversive odor) into the recording chamber.

Light-field deconvolution. The volume reconstruction itself can be formulated as a tomographic inverse problem[27], wherein multi-ple different perspectives of a 3D volume are observed and linear reconstruction methods—implemented via deconvolution—are employed for computational 3D volume reconstruction. The image formation in light-field microscopes involves diffraction from both the objective and microlenses. PSFs for the deconvo-lution can be computed from scalar diffraction theory[28]. More details are given in **Supplementary Note 2**.

After we recorded the raw light-field images, the digital images were cropped to regions of interest (ROIs) and resampled to contain 11 × 11 or 15 × 15 angular light-field samples under each lenslet. Two calibration images, one showing the microlenses with collimated rear illumination and one showing a uniform fluorescent slide, were used for digital image rectification, in which camera pixels are assigned to individual microlenses. Reconstruction of each frame of an image sequence took between 2 and 30 min, depending on the size of the image, number of iterations of the deconvo-lution algorithm, reconstruction method and workstation used. Computational resources are further discussed in **Supplementary Note 2**. A software package for 3D volume reconstruction from light-field images is included as **Supplementary Software**.

Ca^{2+} imaging data analysis. To extract a fluorescence time series for individual neurons from the 4D data, we employed different strategies for *C. elegans* and zebrafish. For *C. elegans*, we first applied rigid-body motion correction to each individual *z*-plane movie. We then computed a median-intensity projection through time for each motion-corrected *z* plane movie and used a maxima-finding algorithm to identify areas of peaked intensity in each projection. A circular ROI was created surrounding each intensity peak, and overlapping ROI areas within *z* planes were eliminated. ROIs in adjacent *z* planes within an *xy* distance of 7 pixels were considered to be a component of the same neuron, up to a maximum of five planes; and for each neuron at each time point, the brightest 100 pixels of the aggregate of all pixels within the neuron's component ROIs were averaged to produce a single fluorescence value and de-trended with an exponential decay function to account for photobleaching. For zebrafish, the data were first de-trended on the basis of the overall intensity of each frame. Then, to reduce time-series data, first we discarded inac-tive voxels on the basis of their time-domain variance. Splitting the volume into smaller subvolumes further reduced data size. We followed the strategy proposed in ref. 20 to extract cellular signals from the Ca^{2+} imaging data. Each subvolume datum underwent PCA/ICA for automated spatial-filter extraction where ideally each spatial filter corresponds to the location of a neuron[20]. After automatically rejecting spatial filters on the basis of size and dis-persion, we applied the spatial filters to the 4D data to extract their fluorescence intensity. Time points during which the fish seemed to contract were discarded and replaced with nearest-neighbor fluorescence intensities. These contractions typically lasted between 200 ms and 1 s only and were temporally very

sparse. Therefore, we regarded them negligible compared to the overall recording time. Fish that moved substantially during image acquisition were discarded from analysis. To extract $\Delta F/F_0$, we calculated $\Delta F/F_0 = 100 \times (F(t) - F_0)/F_0$, with F_0 being the mean fluorescence intensity of each corrected trace.

26. Cold Spring Harbor Laboratory. Hermaphrodite Handbook. *WormAtlas* (ed. Herndon, L.A.) http://www.wormatlas.org/hermaphrodite/hermaphroditehomepage.htm (2014; accessed 20 March 2014).
27. Kak, A.C. & Slaney, M. *Principles of Computerized Tomographic Imaging* (Society of Industrial and Applied Mathematics, 2001).
28. Gu, M. *Advanced Optical Imaging Theory* (Springer, 1999).

Supplementary Information

Simultaneous whole-animal 3D-imaging of neuronal activity using light field microscopy

Robert Prevedel[1-3,10], Young-Gyu Yoon[4,5,10], Maximilian Hoffmann[,1-3], Nikita Pak[5,6], Gordon Wetzstein[5], Saul Kato[1], Tina Schrödel[1], Ramesh Raskar[5], Manuel Zimmer[1], Edward S. Boyden[5,7-9] and Alipasha Vaziri[1-3]

[1]Research Institute of Molecular Pathology, Vienna, Austria.
[2]Max F. Perutz Laboratories, University of Vienna, Vienna, Austria.
[3]Research Platform Quantum Phenomena & Nanoscale Biological Systems (QuNaBioS), University of Vienna, Vienna, Austria.
[4]Department of Electrical Engineering and Computer Science, Massachusetts Institute of Technology (MIT), Cambridge, MA, USA
[5]MIT Media Lab, Massachusetts Institute of Technology (MIT), Cambridge, MA, USA
[6]Department of Mechanical Engineering, Massachusetts Institute of Technology (MIT), Cambridge, MA, USA
[7]Department of Biological Engineering, Massachusetts Institute of Technology (MIT), Cambridge, MA, USA
[8] Department of Brain and Cognitive Sciences, Massachusetts Institute of Technology (MIT), Cambridge, MA, USA
[9] McGovern Institute, Massachusetts Institute of Technology (MIT), Cambridge, MA, USA

[10] These authors contributed equally to this work.

Correspondence should be addressed to E.S.B. (esb@media.mit.edu) or A.V. (vaziri@imp.ac.at).

Supplementary Figures

Supplementary Figure 1. Whole-animal Ca^{2+}-imaging of *C. elegans*.

Supplementary Figure 2. High-resolution images of Fig. 2e and Fig. 2f indicating Neuron ID numbers in z-planes and heatplot map of neuronal activity of all neurons.

Supplementary Figure 3. Identification of neuron classes in *C. elegans* during chemosensory stimulation.
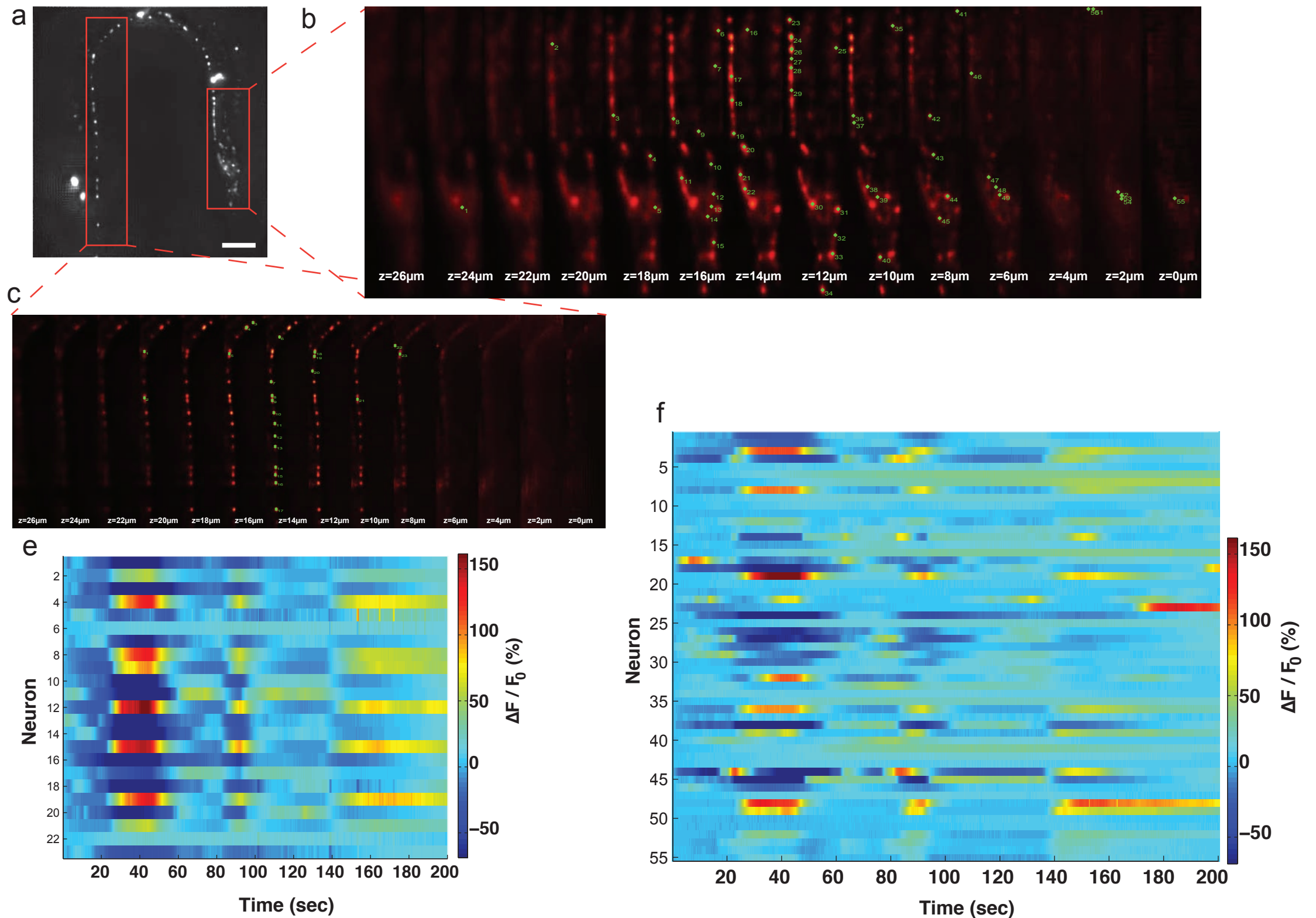
Supplementary Figure 4. High-speed Ca^{2+}-imaging of unrestrained *C. elegans*.

Supplementary Note 1 General principle, optical design choices and their effect on resolution in 3D deconvolution light field microscopy.

Supplementary Note 2 Volume reconstruction for 3D-deconvolution light field microscopy and computing requirements.

Supplementary References

Supplementary Figure 1. Whole-animal Ca²⁺-imaging of *C. elegans*.

Supplementary Figure 1. Whole-animal Ca²⁺-imaging of *C. elegans*.
(**a**) Maximum intensity projection (MIP) of light field deconvolved image (15 iterations) of the whole worm shown in Fig. 2d, containing 14 distinct *z*- planes. Neurons contained in red boxes were further analyzed in (**b-f**). NeuronIDs of *z*-stack in **b** match with heatmap plot of neuronal activity in **f** and show neurons identified in the head using an automated segmentation algorithm, while **c** shows neuronIDs along the ventral cord with corresponding heatplot map shown in **e**. Scale bar 50 μm.

Supplementary Figure 2. High-resolution images of Fig. 2e and Fig. 2f indicating Neuron ID numbers.
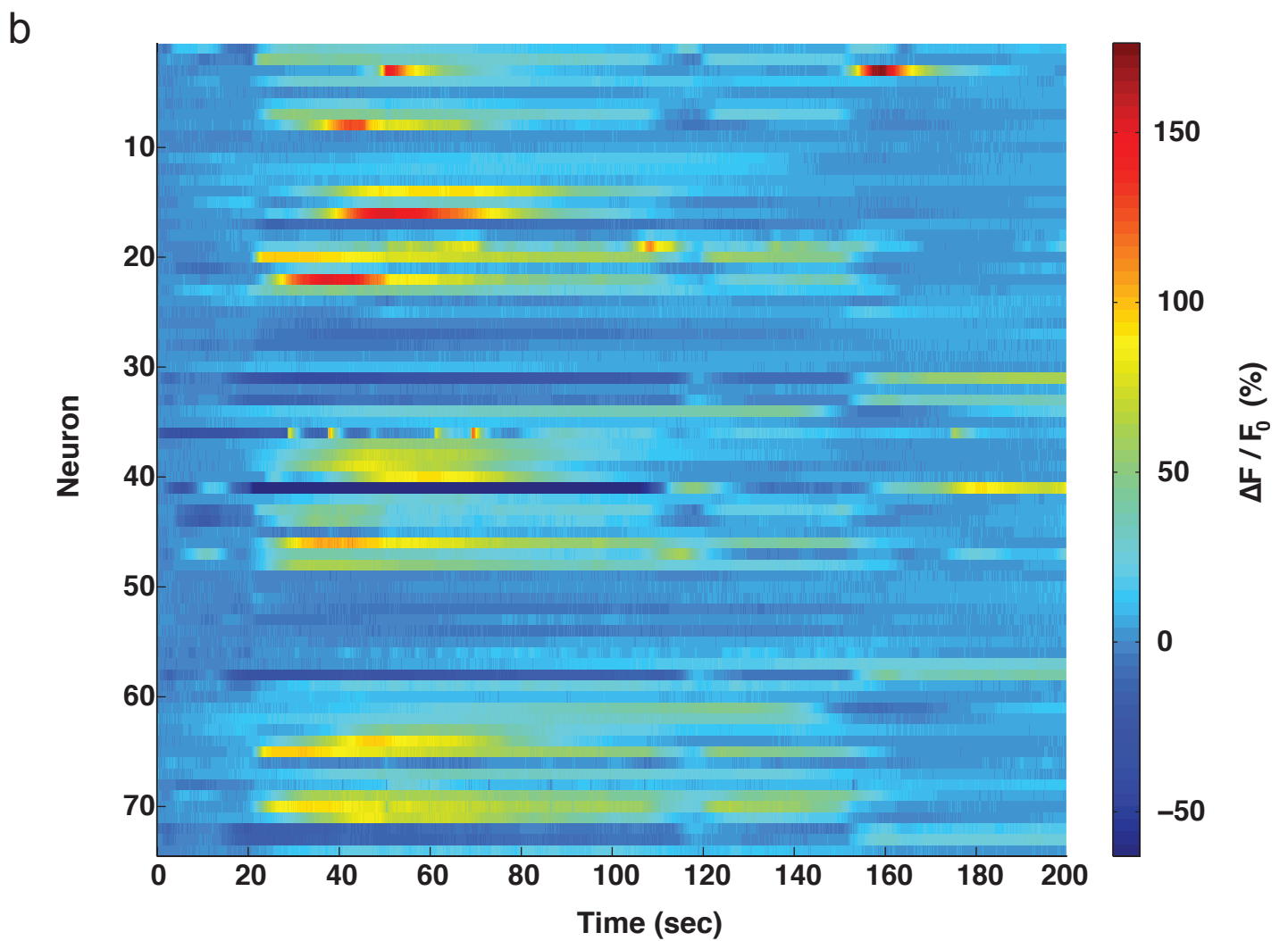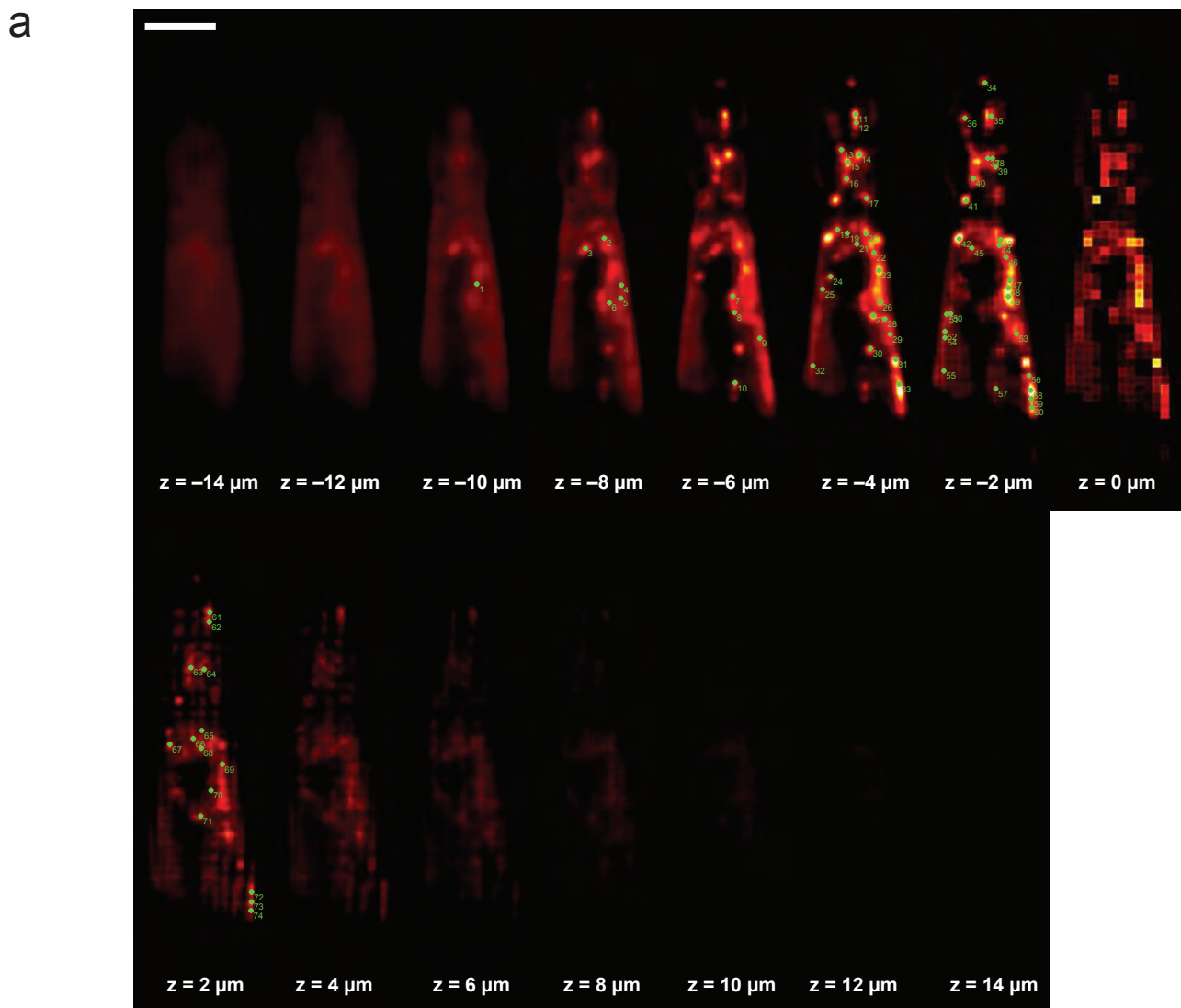
Supplementary Figure 2. High-resolution images of Fig. 2e and Fig. 2f indicating Neuron ID numbers in z-planes in (**a**) and heatmap plot of neuronal activity of all neurons in (**b**).

Supplementary Figure 3. Identification of neuron classes in *C. elegans* during chemosensory stimulation.

Supplementary Figure 3. Identification of neuron classes in *C. elegans* during chemosensory stimulation.

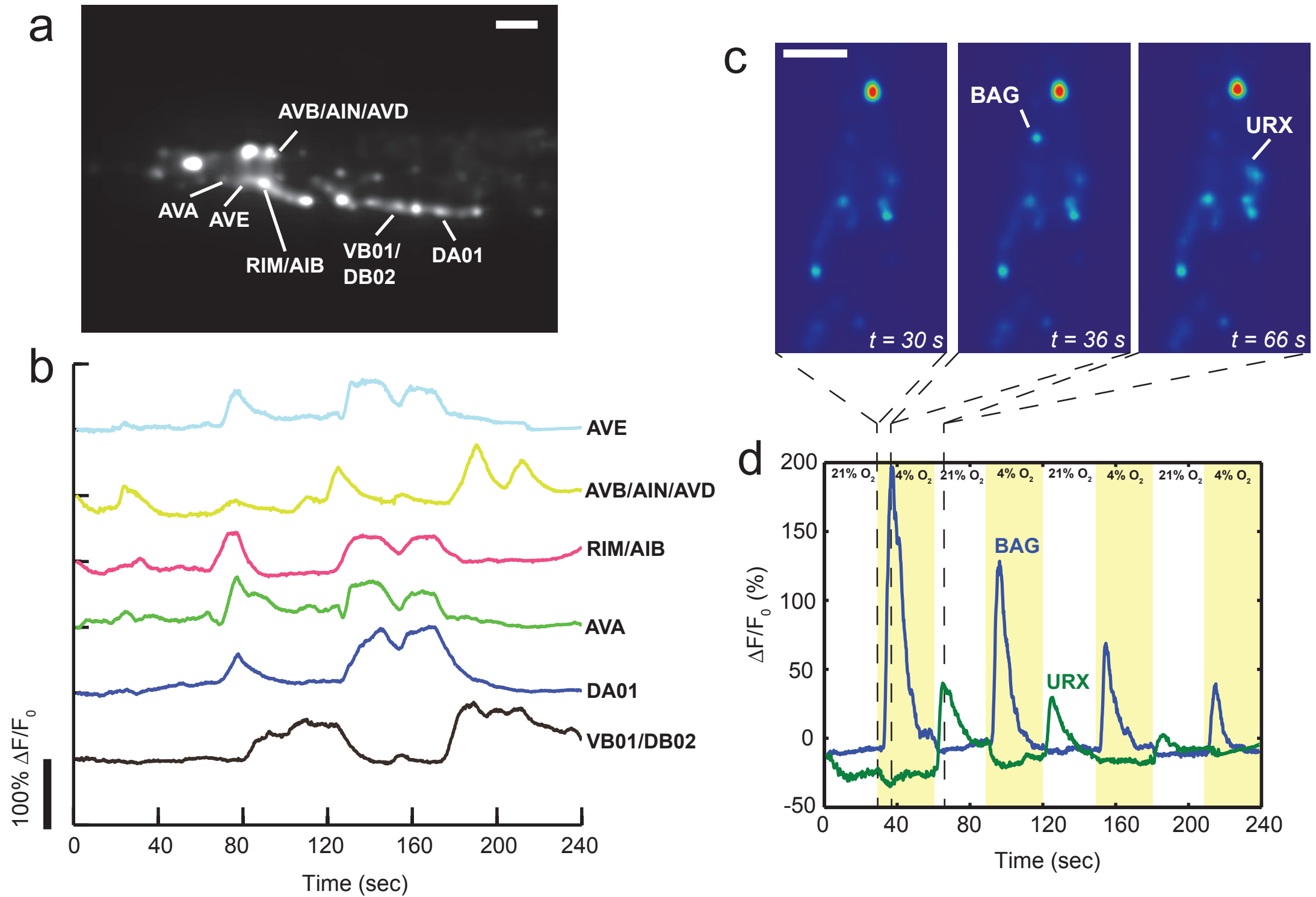Whole brain LFDM recording at 5 Hz of *C. elegans* under consecutively changing O_2 concentrations (30 seconds time-shifts). (**a**) Maximum intensity projection (MIP) of light field deconvolved image (8 iterations) of the worm's head region, containing 7 distinct *z*-planes. Neuron classes were identified based on location and typical Ca^{2+}-signals, whose individual traces are shown in **b**. (**c**) Individual *z*-plane containing the oxygen-downshift sensing neuron BAG at various time-points before, during and after stimulus, respectively. (**d**) Fluorescence traces of oxygen sensory neurons BAG and URX, with varying O_2 concentrations indicated by shading. Scale bar is 20 μm in **a** and **c**.

Supplementary Figure 4. High-speed Ca²⁺-imaging of unrestrained *C. elegans* at 50 Hz.
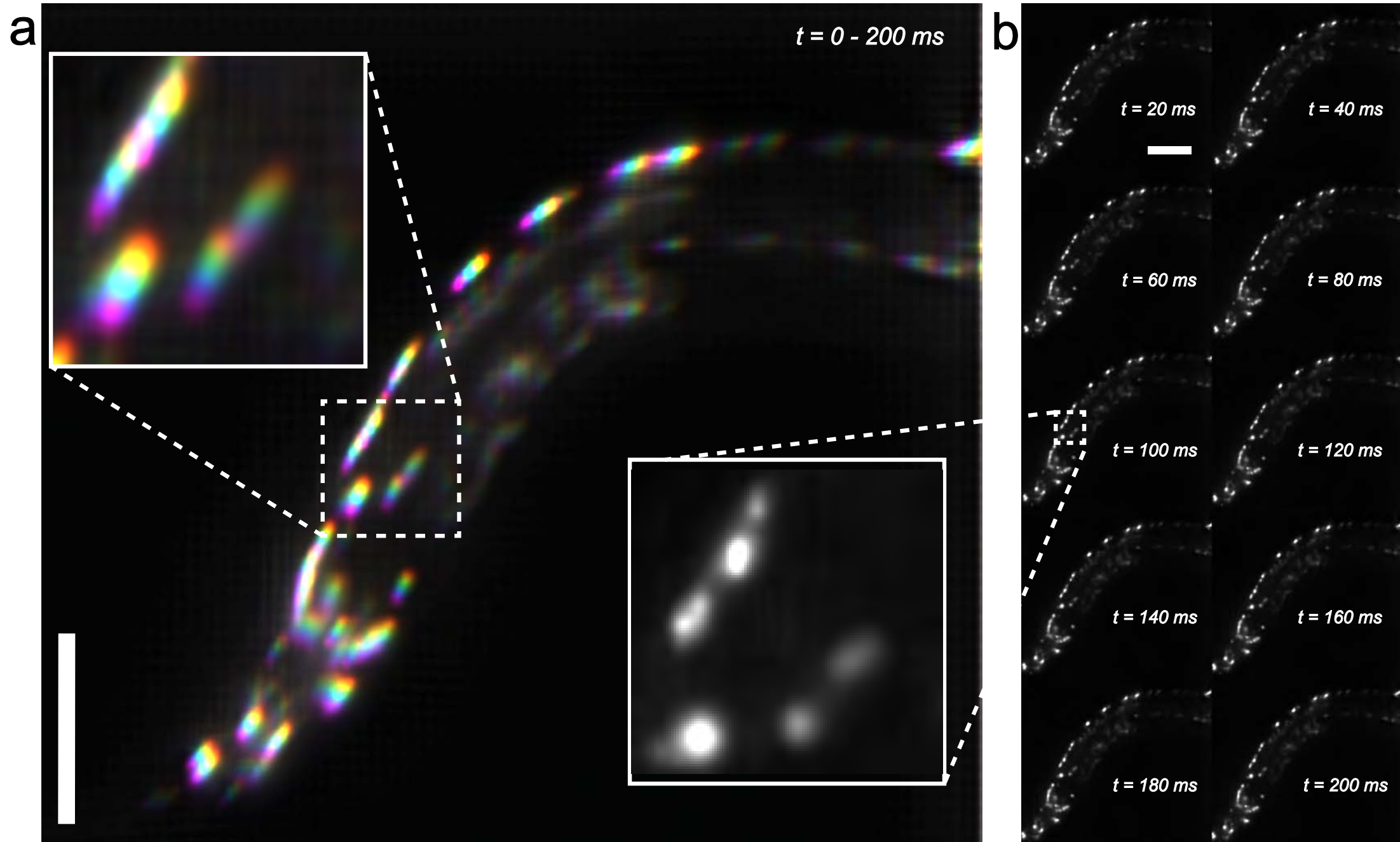
Supplementary Figure 4. High-speed Ca^{2+}-imaging of unrestrained *C. elegans* at 50 Hz. Selected time-series of the LFDM recording of freely-moving worms at 50 Hz shown in **Supplementary Video 4**. (**a**) Overlay of 10 consecutive frames, with colors coding for different time-points. This is equivalent to an effective frame-rate of 5 Hz. At this speed, motion blur would lead to ambiguous discrimination of individual neurons, as is clearly visible in the inset. In contrast, in (**b**) we show the individual frames of the same time-series as recorded with 50 Hz (20 ms exposure time). At this speed, motion blur is almost non-existent. This demonstrates that 50 Hz are sufficient to follow the activity of unrestrained worms, especially if additional worm tracking would be employed. Scale bar is 50 μm in **a** and **b**. Also see **Supplementary Video 3**.

Supplementary Note 1 General principle, optical design choices and their effect on resolution in 3D deconvolution light field microscopy.

Generally speaking, a conventional 2-D microscope captures a high-resolution image of a specimen that is in focus. For volumetric specimens, the same image, however, also contains blurred contributions of areas that are optically out of focus. Unmixing them in post-processing is an ill-posed problem and usually not possible. Scanning microscopes solve this problem by measuring each point in the 3-D volume sequentially. While this is an effective process, it is time-consuming and not always applicable to capturing dynamic events or moving specimens. Light field microscopes change the optical acquisition setup to capture different primitives: instead of recording individual points sequentially, light field microscopes capture "rays" of light, that their summed emission through the 3-D volume. Instead of recording them in sequence, a set of "rays" – the light field – is multiplexed into a single 2-D sensor image. This spatial, rather than temporal, approach to multiplexing drastically improves acquisition speed at the cost of reduced resolution. To recover the 3-D volume from measured emission, a computed tomography problem has to be solved. Following Ref. 1, we implement this reconstruction step as a deconvolution. Please note that while the light field is conceptually comprised of geometric rays, in practice the image formation and inversion also considers diffraction, as discussed in the primary text.

Light field microscopes support all objective magnifications, but usually benefit from a high numerical aperture (NA) and microlenses that are matched with the NA of the employed objective. The choice of objective and microlens array determines the spatial resolution and field-of-view in all three dimensions. The pitch, i.e. the distance between the microlenses, in combination with the sensor's pixel size and objective magnification controls trade-off between spatial resolution vs. field-of-view while the objective's magnification and numerical aperture control axial resolution vs. axial range. Furthermore, the field-number of the microlenses needs to match that of the objective in order to preserve the maximum angular information in the light fields [2].

Due to the variation in sampling density, reconstructed volumes have a lateral resolution that varies along the optical axis. On the focal plane, achievable resolution is equivalent to conventional LFM, i.e. the size of each microlens divided by the magnification of the objective lens (150 μm / 40x = 3.75 μm in our system). The resolution increases for lateral sections close to the focal plane, ~1.5μm laterally in our implementation, but drops at larger distances, e.g. to ~3 μm laterally at -25 μm, in accordance with Ref. [1]. We find similar behavior with the 20x 0.5NA lens used in our zebrafish recordings. Here we find a maximum resolution of ~3.4 μm (~11 μm) laterally (axially) based on a reconstructed point spread function (see also **Fig. 3a**).

It is also possible and straightforward to design microlens arrays for higher magnification objectives in order to look at smaller samples. Following the criteria outlined in Ref. 2, microlenses can be designed taking into account the trade-offs between lateral and axial resolution. For instance we have performed simulations for a 100x 1.4NA oil objective and a f-number matched microlens of 100 μm pitch, and found that our LFDM should have a resolution of ~0.27 μm (1 μm) laterally (axially). The lateral field of view would be 140 μm with a sCMOS camera similar to the one used in this work and we would expect a useful axial range of 10-15 μm.

Supplementary Note 2 Volume reconstruction for 3D-deconvolution light field microscopy and computing requirements.

The software for 3D reconstruction was written in MATLAB (Mathworks) using its parallel computing toolbox to enable multi-core processing, and allows choosing between CPU- and GPU-based executions of the algorithm. The software consists of three different parts: point spread function (PSF) computation, image rectification / calibration, and 3D volume reconstruction. To generate PSFs, we compute the wavefront imaged through the microlens array for multiple points in the volume using scalar diffraction theory [3]. We also exploit the circular symmetry of PSF for its computation, which results in a boost in computational speed. To faithfully represent the high spatial frequency component of the wavefront, computations are performed with a spatial oversampling factor of 3x compared to the size of the virtual pixels that correspond to the resampled image.

For the image rectification and calibration, the size and location of each microlens with respect to the sensor pixels are estimated using calibration images showing a fluorescent slide and a collimated beam. An open source software named LFDisplay [http://graphics.stanford.edu/software/LFDisplay/], for example, can be used to locate the microlenses with respect to the pixels. Once the size and the location of each microlens is determined, captured images are resampled to contain 15 x 15 (11 x 11) angular light field samples under each microlens. The target axial resolution of reconstructed volumes is 2 (4) μm, which requires 12-16 (51) z-slices for worm (zebrafish) samples.

The essential operations for volume reconstruction are based on computing large number of 2-dimensional convolutions. Therefore reconstruction speed depends heavily on the implementation of the convolution operation and its speed. Using the convolution theorem, this problem can be accelerated by computing on graphical processor units (GPUs) in the Fourier domain. The underlying fast Fourier Transform (FFT) can be computed in $O(n \log n)$ operations whereas conventional convolution requires $O(n^2)$ operations. Furthermore, the FFT is well suited for GPU computing, and we found this to result in significant (up to 20x) reduction in computing time compared to 12-core CPU based execution. With GPU computing method, reconstructing individual frames of recorded image sequences using Richardson-Lucy deconvolution method took between 2 and 6 min, depending on the size of the image, on a workstation with one Nvidia Tesla K40c GPU and 128GB of RAM. Specifically, the reconstruction of only the head ganglia region of *C. elegans* (Fig. 2c-e) took about 2 minutes where the reconstruction of the whole C. elegans took about 6 minutes with 8 iterations of the deconvolution algorithm. Similar times were measured for zebrafish volume reconstructions.

In comparison, CPU based computing on 12 parallel cores required between 5 and 30 min. However, by parallelizing the reconstruction on a medium sized cluster employing ~40 nodes, we found that a typical 1000 frame movie of whole *C.elegans* (such as in **Supplementary Video 1**) could be reconstructed within ~12 hours. Cloud based computing options, e.g. through Amazon Web Services and other competing online tools, might also provide efficient means for large-scale volume reconstruction.

Reconstruction times of image sequences could be further optimized by using the reconstructed volume of one frame as the initial guess for the next. This removes the need for multiple algorithmic iterations at each frame and is well-justified because the imaging speed was sufficiently faster than both neuronal activity and movement of the worm.

Supplementary References

1.   Broxton, M. et al., *Optics Express* **21**, 25418 (2013).
2.   M. Levoy, M. et al., *ACM Trans. Graph.* **25**, 924 (2006).
3.   Gu, M. Advanced Optical Imaging Theory, *Springer* **ISBN-10: 981402130X** (1999).